Diploma Thesis

Physics Department

University of Crete

Exploitation of non-linear effects for the discrimination of absorbers in optical resolution photoacoustic microscopy using single wavelength excitation

Supervisors: Prof. Dimitris Charalampidis

Dr. Giannis Zacharakis

Prof. Maria Kafesaki

Research Advisor: Dr. Giorgos Tserevelakis

Krystalia Lemonaki

Heraklion, September 2017

TABLE OF CONTENTS

Περίληψη

Η φωτοακουστική μικροσκοπία οπτικής ανάλυσης (OR-PAM) αποτελεί ένα αποτελεσματικό και λειτουργικό εργαλείο απεικόνισης. Κατά το φωτοακουστικό φαινόμενο, φως απορροφάται από τα μόρια και μετατρέπεται σε θερμότητα. Η επακόλουθη θερμοελαστική διαστολή παράγει ένα ακουστικό κύμα, το οποίο ονομάζεται φωτοακουστικό κύμα. Η ανίχνευση των φωτοακουστικών κυμάτων παρέχει ποσοτικές πληροφορίες σχετικά με τις συγκεντρώσεις διάφορων χρωμοφόρων, όπως οξυγονωμένη και μη οξυγονωμένη αιμοσφαιρίνη ή μελανίνη. Γενικά, το πλάτος του φωτοακουστικού σήματος θεωρείται ότι είναι ανάλογο με το energy fluence του παλμού διέγερσης. Ωστόσο, καθώς αυξάνεται η ένταση της ακτινοβολίας της πηγής διέγερσης, η εξάρτηση του συντελεστή θερμικής διαστολής από τη θερμοκρασία και ο κορεσμός του συντελεστή απορρόφησης έχει ως αποτέλεσμα μία μετρήσιμη μη γραμμική εξάρτηση του φωτοακουστικού σήματος από την ένταση της προσπίπτουσας ακτινοβολίας. Η μη γραμμικότητα στη φωτοακουστική μικροσκοπία έχει χρησιμοποιηθεί πρόσφατα σε διάφορες εφαρμογές όπως η διαφοροποίηση οπτικών απορροφητών και η μέτρηση του κορεσμού οξυγόνου στα αγγεία in vivo.

Σε αυτή την εργασία, θεωρούμε τη μη γραμμικότητα στη φωτοακουστική μικροσκοπία ως ένα υποψήφιο μηχανισμό για τη διάκριση μεταξύ δύο διαφορετικών τύπων οπτικών απορροφητών. Πιο συγκεκριμένα, διερευνούμε πειραματικά τη γένεση μη γραμμικών φωτοακουστικών σημάτων ως ένα μέσο για το διαχωρισμό του αίματος από το μελάνι, χρησιμοποιώντας ακτινοβολία παλμικού λέιζερ στα 532 nm. Επομένως, χρησιμοποιώντας αυτή την εναλλακτική προσέγγιση, αποδείχθηκε ότι μπορεί να επιτευχθεί ένας αξιόπιστος διαχωρισμός με χρήση ενός μήκους κύματος διέγερσης, σε αντίθεση με τις κλασικές τεχνικές διαχωρισμού απορροφητών που απαιτούν δύο διαφορετικά μήκη κύματος για τον ίδιο σκοπό. Η προτεινόμενη μέθοδος θα μπορούσε να αξιοποιηθεί σε εφαρμογές όπως ο διαχωρισμός αιμισφαιρίνης από μελανίνη, αναβαθμίζοντας την τεχνικής της φωτοακουστικής μικροσκοπίας οπτικής ανάλυσης με ένα απλό, χαμηλό σε κόστος αλλά πάνω απ'όλα αγιόπιστο τρόπο.

Abstract

Optical resolution photoacoustic microscopy (OR-PAM) is an effective *in vivo* functional imaging tool. During photoacoustic (PA) effect, light is absorbed by molecules and converted into heat. Subsequent thermoelastic expansion generates an acoustic wave, termed as the PA wave. Detection of PA waves provides quantitative information about the concentrations of multiple chromophores such as oxygenated and deoxygenated hemoglobin molecules in red blood cells and melanin. Generally, the amplitude of the PA signal is assumed to be linearly proportional to the excitation pulse fluence. However, as the excitation laser intensity increases, the temperature dependence of thermal expansion coefficient results in a measurable nonlinear dependence of the PA signal on the excitation pulse fluence. PA nonlinearity has recently been used in several applications such as quantifying picosecond absorption relaxation times with a nanosecond laser, differentiating optical absorbers, measuring oxygen saturation in vivo, and performing label-free PA nanoscopy of biological structures having undetectable fluorescence.

In this work, we consider photoacoustic nonlinearity as a candidate mechanism to discriminate between two different types of optical absorbers. More specifically, we experimentally investigate nonlinear photoacoustic signal generation as a means of unmixing blood and ink, by employing pulsed laser radiation at 532 nm. Therefore, using this alternative approach, it was demonstrated that an accurate absorber differentiation can be achieved through single wavelength excitation, unlike the conventional linear unmixing methods requiring two different wavelengths for such a purpose. The proposed methodology could find several applications regarding the specific imaging of biological components presenting discrete nonlinear PA behavior, such as melanin and hemoglobin, upgrading significantly the potential of OR-PAM technique in a simple, low-cost and reliable manner.

1. Introduction

1.1 Photoacoustic imaging

Photoacoustic imaging is a relatively new modality that has been kicked off in the mid 1990's by technological advances in the fields of laser sources and ultrasound detection. [1] The photoacoustic imaging technique is based on the photoacoustic effect and is schematically illustrated in Figure 1.
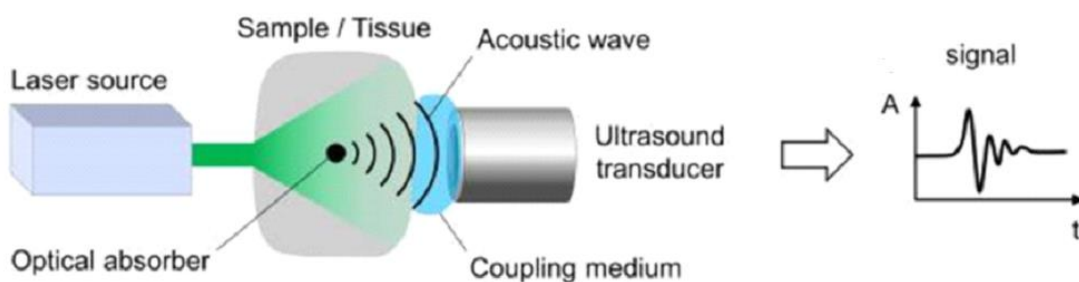

Figure 1: Principle of photoacoustic imaging [1].

Typically, the sample is illuminated by a pulsed laser using short nanosecond pulses in the visible or near-infrared spectral range. The laser pulses propagating through the tissue establish a time-varying electromagnetic field, which is partially absorbed by certain chromophores. Part of the absorbed light energy is converted into heat, leading to a transient local temperature rise (usually < 0.1 °C) and generating an initial build-up of pressure through thermoelastic expansion. This generated pressure propagates through the sample in form of a broadband acoustic wave, which is detected by an ultrasound transducer.

Photoacoustic imaging can be divided into several categories: PA Tomography (PAT), PA microscopy and its variants. [2] PAT can perhaps be regarded as the traditional model of PA imaging as envisaged by early practitioners. It is also the most general and least restrictive PA imaging approach with the fewest limitations on imaging performance imposed by its practical implementation.

In PAT, full field illumination, in which a large diameter pulsed laser beam irradiates the tissue surface, is employed. At NIR wavelengths where tissue is relatively transparent, the light

penetrates deeply and is also strongly scattered, resulting in a relatively large tissue volume becoming 'bathed' in diffuse light. Absorption of the incident radiation by tissue chromophores leads to impulsive heating of the irradiated tissue volume followed by the rapid generation of broadband ultrasonic waves. These propagate to the tissue surface where they are detected by a mechanically scanned ultrasound receiver or array of receivers. The time-varying ultrasound signals can then, with knowledge of the speed of sound, be spatially resolved and back projected to reconstruct a three-dimensional image.
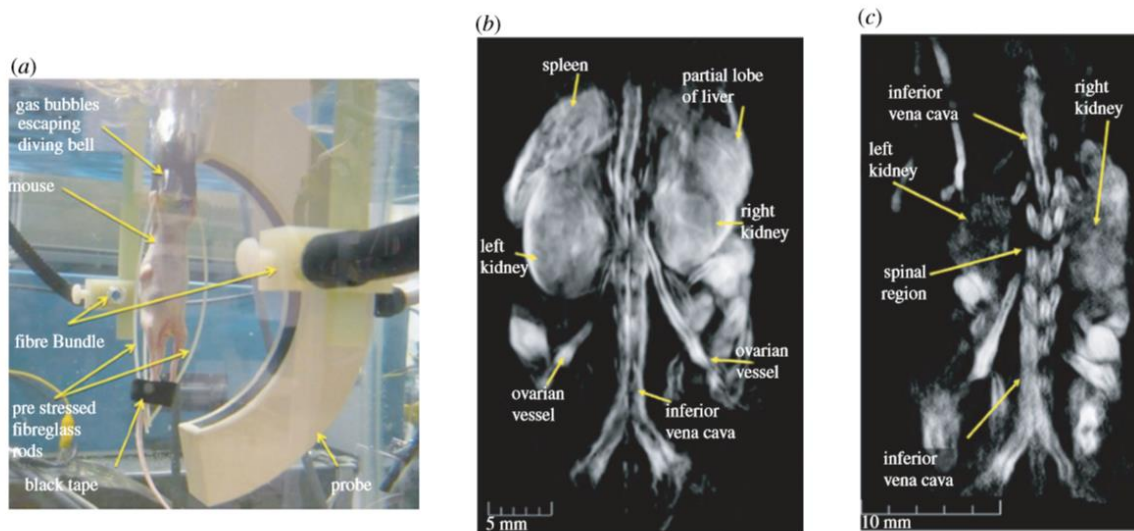
Figure 2: PAT whole body small animal scanner. [3] (a) Experimental arrangement. (b) Three-dimensional image of a nude mouse illuminated at 755 nm. Both kidneys are visualized as well as the spleen and a partial lobe of the liver. (c) Image showing spinal region and left and right kidneys.

PA microscopy refers to techniques in which a PA image is obtained by raster scanning either a focused ultrasound detector or a focused laser beam. The image is then formed directly from the set of acquired A-lines, without the aid of a reconstruction algorithm as in PAT. If a focused ultrasound detector is used, it is termed acoustic resolution PA microscopy (AR-PAM) since axial and lateral spatial resolution is defined by the physics of ultrasound propagation and detection. If a focused laser beam is used, it is termed OR-PAM since the spatial resolution in at least one plane, usually the lateral, is defined by the spatial characteristics of a focused laser beam propagating in tissue. Despite the name, PAM, unlike its optical equivalent, does not necessarily imply the observation of anatomy on a small length scale. AR-PAM for example, can be used to image to depths of several mm, at the cost of a reduced spatial resolution.

The term AR-PAM is typically used to describe implementations that employ a single mechanically translated or rotated focused transducer to map the PA signals. To acquire a three-dimensional image, both the transducer and the excitation beam are mechanically scanned together over a planar surface, generating and detecting PA waves at each step of the scan. The resulting two-dimensional sequence of detected acoustic signal or A-lines, each of which represents a depth profile of absorbed energy, is then rectified, envelope detected, spatially resolved and mapped to a grayscale to form a three-dimension image directly.
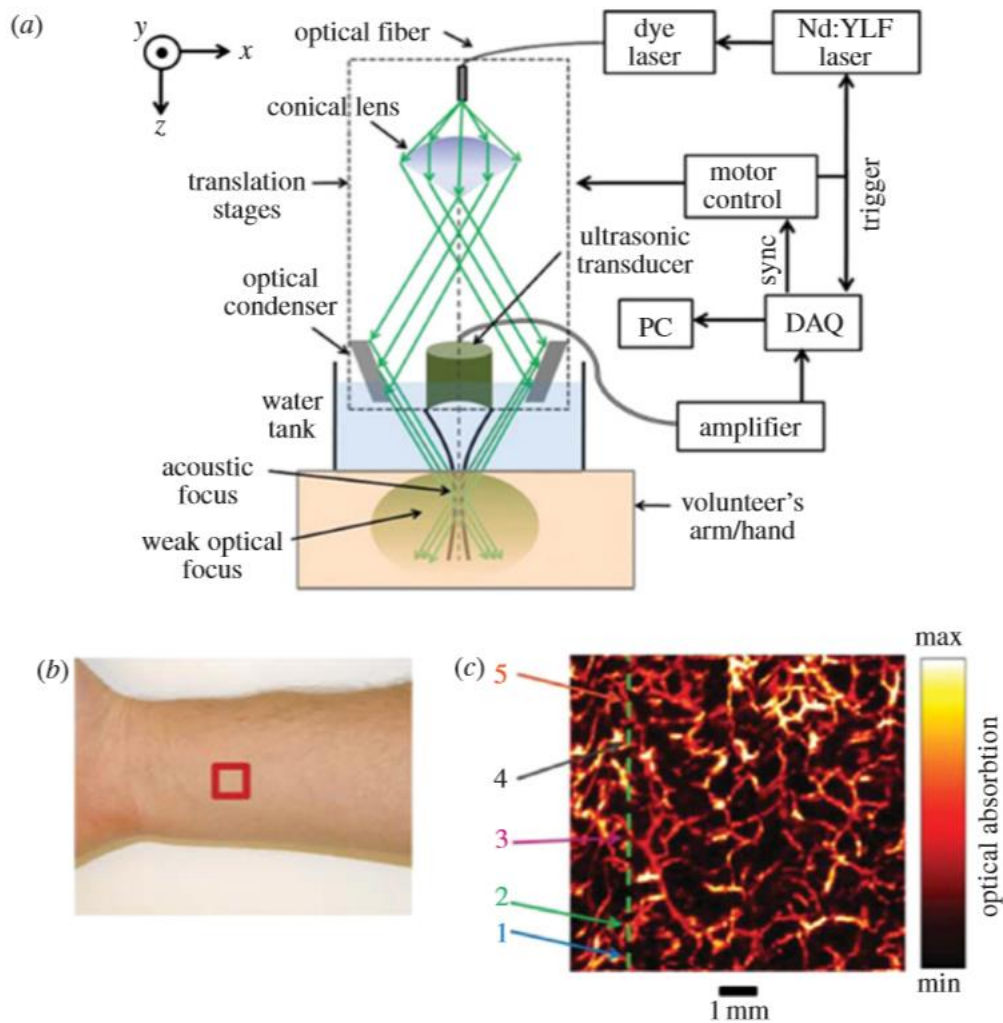
Figure 3: Acoustic-resolution photoacoustic microscopy (AR-PAM) system used for imaging the skin vasculature. [4] (a) Schematic of system, (b) region of forearm scanned, (c) lateral x–y Maximum Amplitude Projection (MAP) image

In OR-PAM, the lateral resolution is defined by the dimensions of a tightly focused diffraction limited laser beam which is used to generate the PA waves. Also in common with optical microscopy, it is a strictly superficial imaging technique with a maximum penetration depth of approximately 1 mm in most tissues due to optical scattering. However, an important distinguishing feature is that unlike any of the current variants of optical microscopy, it provides optical absorption-based image contrast.
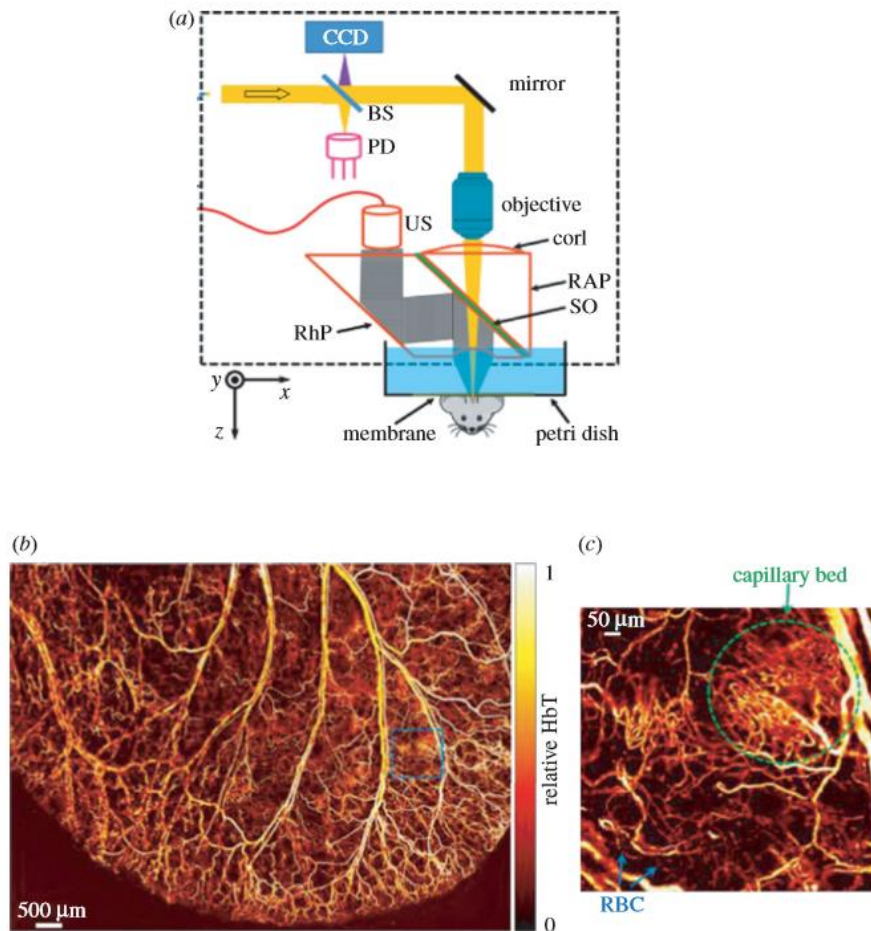
Figure 4: Optical-resolution photoacoustic microscopy (OR-PAM) scanner used for in vivo imaging of the mouse ear. [5] (a) Schematic of system. (b) In vivo image of the microvasculature in the mouse ear. (c) Expanded region shows capillary network and red blood cells (RBC) within a capillary.

Figure 4 shows a schematic of one implementation. A high numerical aperture optical lens is used to focus the excitation laser beam onto the tissue surface and an optically transparent acoustic reflector directs the PA waves to an ultrasound transducer. By raster-scanning the

focused excitation beam and the transducer together and recording the detected A-lines at each point, a three-dimensional image can be formed as in AR-PAM. However, unlike, AR-PAM, lateral resolution for depths less than approximately 1 mm (beyond this optical scattering defocuses the beam and degrades resolution) is defined by the diffraction limited dimensions of the focused laser beam. Compared with AR-PAM much higher lateral resolution of the order of a few microns can therefore be achieved over this depth range. To achieve a comparable acoustic diffraction limited resolution with AR-PAM would require a broadband acoustic frequency content extending to several hundred MHz. Although it is possible to generate PA waves with such a broad bandwidth, acoustic attenuation at such high frequencies is much higher than optical attenuation and would limit penetration depth to approximately 100 μm. By contrast, in OR-PAM the maximum penetration depth of approximately 1mm is a consequence not of optical or acoustic attenuation but the spreading and distortion of the excitation laser beam owing to tissue optical scattering which prevents a high focus from being maintained beyond this depth.

1.2 Spectroscopic photoacoustic imaging

The optical absorption spectra of the tissue components and contrast agents vary greatly with optical wavelength. [6] Therefore, spectroscopic methods can be used to unmix the signals from different optical absorbers in a photoacoustic image and provide an estimation of their concentrations. This technique is known as spectroscopic PA (sPA) imaging. sPA imaging allows for accurate measurement of blood oxygenation saturation (SO_2) or nanoparticle deposition in tissue.

A number of methods have been proposed to spectrally unmix absorbers in PA images [7]. One simple spectroscopic method uses the PA signals acquired at two optical wavelengths. These signals are then used to estimate either SO_2 or the state of an activatable contrast agent. Multispectral optoacoustic tomography (MSOT) can distinguish the activated probe, over both slowly varying spectra of the background and the inactive probe, by acquiring photoacoustic data at several wavelengths and analyzing spectral contributions on a per-pixel bases, i.e.,

$$\mu_a^j(\lambda) = \varepsilon_a(\lambda)c_a^j + \varepsilon_i(\lambda)c_i^j + B(\lambda) \quad \textit{1.2.1}$$

Where $\mu_a^j(\lambda)$ is wavelength-dependent absorption in pixel j as reconstructed by optoacoustic tomography, $B(\lambda)$ is contribution of background chromophores, $\varepsilon_a(\lambda)$, $\varepsilon_i(\lambda)$, c_a^j, and c_i^j are extinction of activated and inactive probe and their spatial distribution on a per pixel basis.

Figure 5 demonstrates basic validation measurements that summarize and explain the MSOT ability to detect probe enzymatic activation [7]. Figure 5 (a) plots measurements of the spectral extinction characteristics of the inactive (dotted line) and activated (solid gray line) forms of the MMPSense™ 680 probe while the spectra of oxy- and deoxyhemoglobin is also shown for reference purposes. An enabling feature for the method developed, is the characteristic spectral change of the extinction (absorption) coefficient between activated and non-activated states, in the far-infrared portion of the spectrum between 635 and 675 nm, shown in greater detail in the insert of Figure 5 (a) To test the methodology, the tissue-mimicking (scattering and absorbing) phantom with insertions containing activated and inactive MMPSense probe was imaged by both MSOT and epi-fluorescence. While spectral changes between active (circular insertion on the right) and inactive (insertion on the left) are not clearly distinguishable at the representative single wavelength reconstructions of Figure 5 (b) (made at 635 nm) and Figure 5 (c) (675 nm) of the phantom imaged, multispectral processing accurately reveals the different states between the left and right tubes in Figure 5 (d) and (e) shows a corresponding 'top-view' planar fluorescence image of the phantom, made after the MSOT measurements, showing strong fluorescence from the insertion containing the activated probe. Interestingly, light diffusion through the phantom causes the appearance of background diffusive fluorescence signal on Figure 5 (e), which is absent from the reconstructed MSOT images of Figure 5 (d) due to the high-resolution three-dimensional imaging capabilities of the method, not affected by light diffusion. Finally, Figure 5 (f) offers an independent confirmation of the MMPSense activation by trypsin and the fluorescence signal changes observed by direct imaging of activation in two transparent tubes, without surrounding diffusive medium.
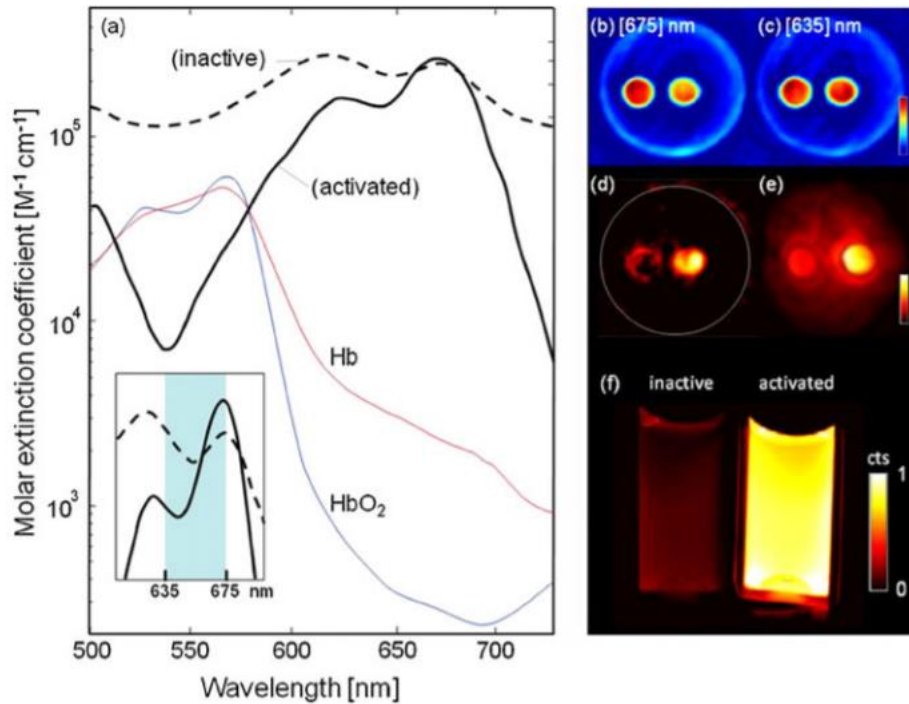
Figure 5: a) Measured spectral extinction characteristics of inactive (dotted line) versus activated (solid gray line) MMPSense™ 680 probe [7]. Spectra of oxy- and deoxyhemoglobin are also shown for reference. Inset: zoom-in from the wavelength range that was used for MSOT imaging. b) Optoacoustic image of phantom with MMPSense™ insertions at 635 nm excitation. Circular insertion containing activated probe is on the right while the inactive insertion is on the left c) Corresponding optoacoustic image at 675 nm excitation. d) Multispectrally resolved (MSOT) image resolving the distribution of activated probe inside the phantom e) Planar (top view) fluorescence image of the phantom performed after MSOT imaging sessions, confirming fluorescence from the activated probe f) Planar fluorescence image comparing inactive (left) and active MMPSense™.

An alternative approach, which treats each pixel as a linear combination of absorbers, provides a more realistic model [8]. Thus, each pixel can contain multiple absorbers and the relative contribution of each absorber to the overall spectrum can be estimated. A linear model is then used to calculate the absorber concentrations in each pixel while minimizing the mean squared error.
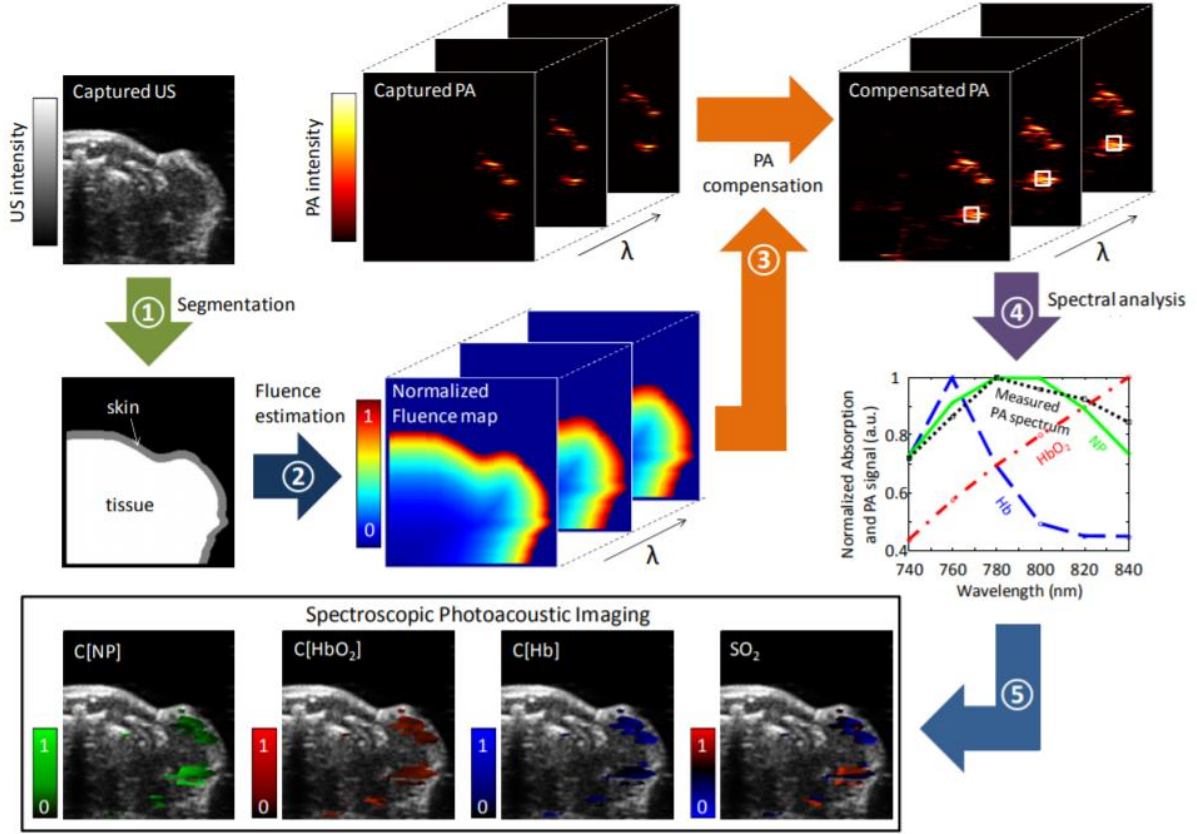
Figure 6: Schematic diagram of the developed spectroscopic photoacoustic imaging algorithm [8].

Assuming there are three major optical absorbers in a body (i.e., oxyhemoglobin (HbO_2), deoxyhemoglobin (Hb), and nanoparticle (NP)), the absorption coefficient of localized mouse tissue can be defined by the sum of absorption coefficients for HbO_2, Hb, and NP in the region. Given depth- and wavelength-dependent fluence compensation, the measured local PA spectrum p_0 can be directly related to the local absorption spectrum μ_a:

$$p_0(\lambda) = \Gamma(\lambda) \cdot \mu_a(\lambda) \cdot F(\lambda) \quad 1.2.2$$

where Γ is the local Grüneisen parameter and F is wavelength-dependent local laser fluence.

Then the concentrations of multiple absorbers can be resolved, and therefore distinguish tissue components. Moreover, the resolved HbO_2 and Hb concentrations can be used for estimating oxygen saturation in blood.

Generally, photoacoustic signals can be used to derive a number of physical, chemical and functional parameters of the absorber and its microenvironment [9]. Since a single parameter

may not be able to fully reflect the true physiological and pathological conditions, multi-parameter PAM can provide a more comprehensive understanding, thus benefiting the diagnosis, staging and treatment of diseases. Total concentration of hemoglobin (C_{Hb}), for example, is the most commonly used blood perfusion index. At the isosbestic wavelengths of hemoglobin (e.g., 498 nm, 568 nm and 794 nm), the PA signal amplitude reflects the C_{Hb} distribution in relative values, regardless of the oxygenation level of hemoglobin (Figure 9a). From fluence-compensated PAM measurements at two or more wavelengths, the relative concentrations of the two forms of hemoglobin (oxy-hemoglobin and deoxy-hemoglobin) can be quantified through spectral analysis, and thus sO_2 can be computed (Figure 9b). More specifically, the intensity of each pixel for a single excitation wavelength λ depends on: the relative concentration for oxy- and deoxy-Hb (percentage %) C, the absorption coefficient for each component μ(λ) and the local excitation intensity I(λ), which is mathematically described as:

$$P(\lambda) = C_{oxy} * \mu_{oxy}(\lambda) * I(\lambda) + C_{deoxy} * \mu_{deoxy}(\lambda) * I(\lambda) \quad 1.2.3$$

A system of two equations, which can be solved for C_{oxy} and C_{deoxy} and generate a multicolor image.
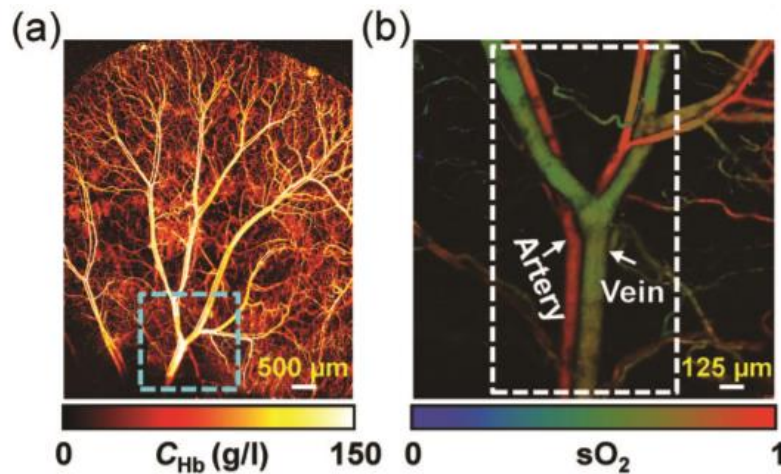
Figure 7: (a) OR-PAM of the total concentration of hemoglobin in a mouse ear. (b) Multicolor image of the oxygen saturation of hemoglobin in the area indicated by the dashed box in (a) [9].

In each aforementioned method, the choice of optical wavelengths is critically important. The unique spectral features of each absorber must be captured by a discrete set of wavelengths.

Ideally, a large number of wavelengths spanning a broad spectrum should be used. In practice, the number of wavelengths that can be used is limited by a number of factors, including the linewidth of the laser, the spectral range of the laser, the spectral-dependent attenuation of light in tissue, and the pulse repetition rate of the laser. Each imaging wavelength further decreases the temporal resolution, thereby increasing the overall imaging time and the likelihood of introducing motion artifacts, which can be detrimental to spectral unmixing. Here, in our study, we propose a new method for discrimination of different optical absorbers, based on their nonlinear response, while energy fluence increasing with the great advantage of using single laser excitation.

2. Theory

2.1 The Photoacoustic (PA) effect

The production of ultrasonic waves from absorption of electromagnetic radiation, known as the photoacoustic effect (Figure 7), is generally described as arising from a linear thermal expansion mechanism. [10] The optical deposition of energy causes a heating and thermal expansion of the absorber, the motion from expansion acting as a source for the production of sound waves. Since acoustic radiation is emitted wherever heat is deposited, the spatial and temporal character of emitted acoustic wave necessarily carries information about the geometry and optical properties of the absorber. In order to obtain this effect the light intensity must vary, either periodically (*modulated light*) or as a single flash (*pulsed light*). The photoacoustic effect is quantified by measuring the formed pressure changes with appropriate detectors, such as transducers. The time variation of the electric output (current or voltage) from these detectors is the photoacoustic signal. Typically, light in the visible or near-infrared spectrum (400 nm–1,200 nm) is used for excitation of PA responses due to the relatively weak absorption of biological tissues in this spectral region, also known as the optical window. For biomedical applications, examples of usable contrast include intrinsic chromophores (e.g., hemoglobin in its oxygenated and deoxygenated form, melanin, fat), extrinsically administered agents (e.g., nanoparticles, fluorophores) or genetically encoded markers, such as fluorescent proteins.
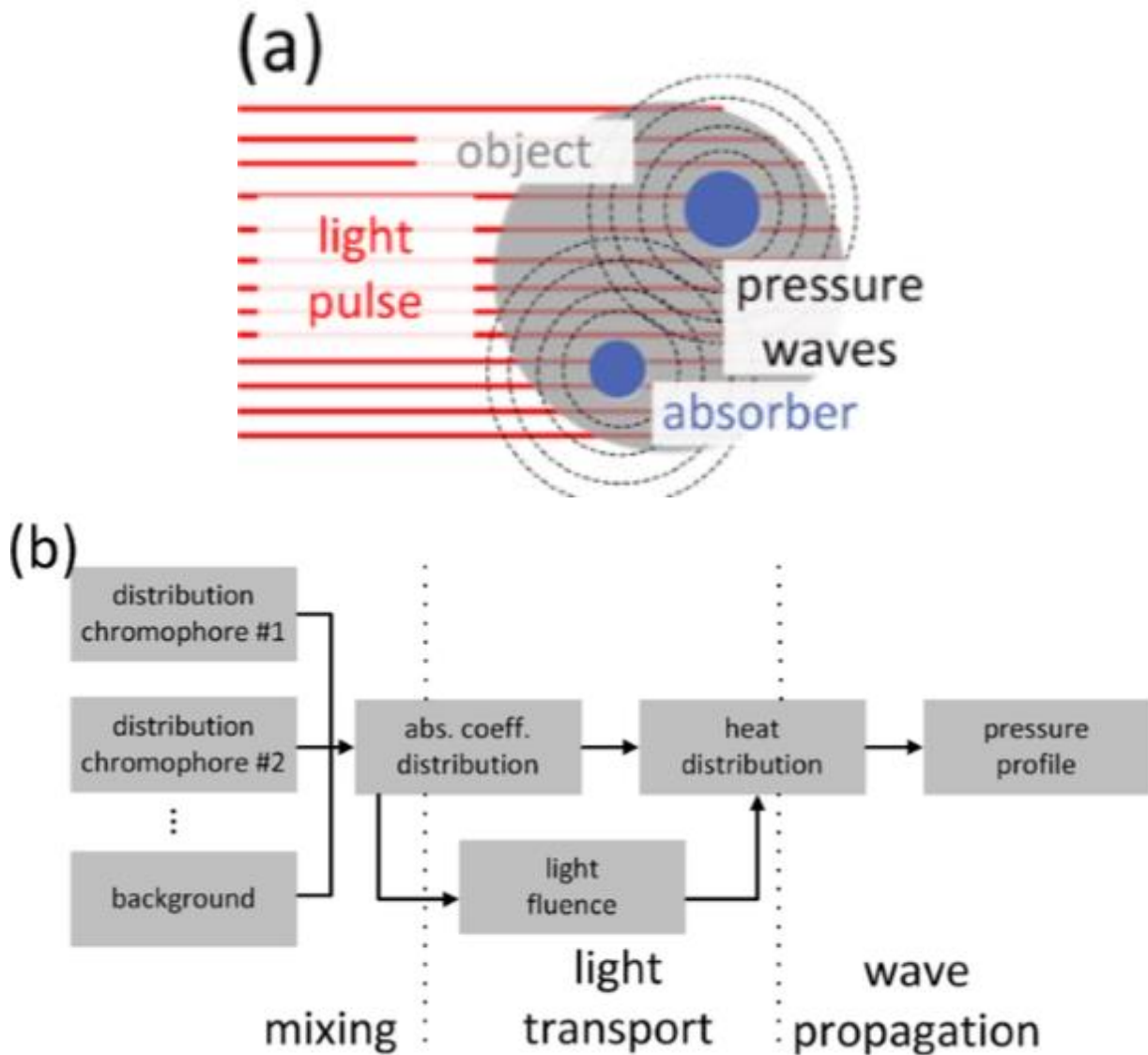
Figure 7: (a): Illustration of the optoacoustic effect. The object is illuminated with a light pulse and photons are absorbed within the object [10]. The optical energy is converted to mechanical energy and gives rise to propagating pressure waves (b): Schematic of the main physical processes involved in photoacoustic imaging: The distributions of different chromophores contribute to optical absorption and they mix to the spatially varying absorption distribution. The transport of light determines the local heat distribution by both absorption distribution and light fluence. The deposited heat excites pressure waves which propagate to the detectors' locations according to acoustic wave equation

2.2 Derivation of the general photoacoustic equation

In order to derive the general photoacoustic equation, we begin with two basic equations [11]. The first one is the thermal expansion equation

$$\nabla \cdot \vec{\xi}(\vec{r},t) = -\kappa p(\vec{r},t) + \beta T(\vec{r},t) \quad (2.2.1)$$

where vector $\vec{\xi}$ denotes the medium displacement from the equilibrium state, κ is the isothermal compressibility (typical value for soft tissue $\sim 5\text{x}10^{-10}\,\text{Pa}^{-1}$), β is the thermal coefficient of volume expansion (typical value for muscle $\sim 4\text{x}10^{-4}\,\text{K}^{-1}$) and p, T are the pressure and temperature functions respectively. Thermodynamically, κ is defined as

$$\kappa = -\frac{1}{V}\left(\frac{\partial V}{\partial P}\right)_T \quad (2.2.2)$$

and corresponds to the fractional change of volume while changing the pressure at a constant temperature

and β as

$$\beta = \frac{1}{V}\left(\frac{\partial V}{\partial T}\right)_P \quad (2.2.3)$$

expressing the fractional change of volume while changing temperature at a constant pressure.

Equation (1.1.1) describes that the fractional volume expansion of the medium (left part) is equal to the sum of two factors (right part): the first one is related to the exerted pressure, whereas the second one is a function of the object's temperature. Positive pressures tend to "shrink" the object –this explains the minus sign of the first term. On the other hand, the second factor expresses a linear relation of the volume expansion with the temperature -the more the object is heated the more it will expand.

The second basic equation is actually another version of the Newton's second law called inviscid force equation and has the form

$$\rho\frac{\partial^2}{\partial t^2}\vec{\xi}(\vec{r},t) = -\nabla p(\vec{r},t) \quad (2.2.4)$$

The left term here represents the mass density times the acceleration and the right one is the force applied per unit volume. In order to make clearer why the gradient of the pressure is related

to the force, let us take the following example: Consider a cubic parcel of a medium with mass given by the following equation

$$m = \rho \cdot dA \cdot dz \quad (2.2.5)$$

where dA is the respective surface area and dz its height. By employing Newton's second law, we can examine a pressure difference dP (assumed to be only in z direction) to find the resulting force as

$$F = m \cdot a = \rho \cdot dA \cdot dz \cdot a = -dp \cdot dA \quad (2.2.6)$$

The latter relation can be rewritten as

$$\rho \alpha = -\frac{dp}{dz} \quad (2.2.7)$$

or in a more general form as

$$\rho \vec{\alpha} = -\nabla \vec{p} \quad (2.2.8)$$

which comprises a compact form for the initial equation (2.2.4).

Taking the divergence of (1.1.4), we obtain

$$\rho \frac{\partial^2}{\partial t^2} [\nabla \cdot \vec{\xi}(\vec{r},t)] = -\nabla^2 p(\vec{r},t) \quad (2.2.9)$$

Substituting $\nabla \cdot \vec{\xi}(\vec{r},t)$ from (1.1) into (1.1.9), we get

$$\rho \frac{\partial^2}{\partial t^2} [-\kappa p(\vec{r},t) + \beta T(\vec{r},t)] = -\nabla^2 p(\vec{r},t) \quad (2.2.10)$$

or by re-arranging the terms

$$\left(\nabla^2 - \rho \kappa \frac{\partial^2}{\partial t^2} \right) p(\vec{r},t) = -\beta \rho \frac{\partial^2 T(\vec{r},t)}{\partial t^2} \quad (2.2.11)$$

In general, the speed of sound is given by the Newton-Laplace equation

$$u_s = \sqrt{\frac{K}{\rho}} \quad (2.2.12)$$

where K is the bulk modulus measuring the resistance of the medium to uniform compression, which is equal to the inverse compressibility κ (isothermal). Therefore, the speed of sound can be expressed as

$$u_s = \sqrt{\frac{1}{\rho\kappa}} \quad (2.2.13)$$

By combining (1.1.11) and (1.1.13), we get the general photoacoustic equation with a final form

$$\left(\nabla^2 - \frac{1}{u_s^2}\frac{\partial^2}{\partial t^2}\right)p(\vec{r},t) = -\frac{\beta}{\kappa u_s^2}\frac{\partial^2 T(\vec{r},t)}{\partial t^2} \quad (2.2.14)$$

The left-hand side of the equation describes the pressure wave propagation whereas the right-hand side represents the source term. Therefore, time-invariant heating does not produce a pressure wave; only time-variant heating does.

2.3 Photoacoustic equation under thermal confinement

To simplify the model of the induced pressure variations, two assumptions are usually made on the duration of the laser pulse: the first is the so-called thermal confinement assuming that the heat conductance during a laser pulse in one image voxel does not affect the neighboring voxels ($\tau \ll \frac{\Delta l}{4D_t}$, where Δl is the dimension of the voxels and D_t is the thermal diffusivity). The second is the so-called stress confinement assuming the volume expansion during the laser pulse to be negligible ($\tau \ll \frac{\Delta l}{u^s}$). With these simplifications, we can derive from the fundamental equation

$$Q = mC_V\mathrm{T} \quad (2.3.1)$$

where Q is the thermal energy, m is the mass, C_V (J/kg·K) is the specific heat capacity under constant volume and T is the absolute temperature that

$$\frac{dQ}{dt} = mC_V\frac{dT}{dt} = \rho VC_V\frac{dT}{dt} \quad (2.3.2)$$

If we define a heating function H as the thermal energy converted per unit volume per unit time (units: J/m^3/s), then we have from (2.3.2) that

$$H = \rho C_V \frac{dT}{dt} \quad (2.3.3)$$

Laws of thermodynamics also indicate that

$$\frac{C_P}{C_V} = \frac{\kappa}{\beta_S} \quad (2.3.4)$$

where C_P and C_V are the specific heat capacities under constant pressure and volume, whereas β_S stands for the isoentropic compressibility, defined as

$$\beta_S = -\frac{1}{V}\left(\frac{\partial V}{\partial P}\right)_S \quad (2.3.5)$$

expressing the fractional change of volume while changing the pressure at a constant entropy.

On the other hand, the equation of state denotes that

$$u_s^2 = \left(\frac{\partial P}{\partial \rho}\right)_S \quad (2.3.6)$$

By combining (1.2.5) and (1.2.6) we get

$$
\begin{aligned}
\beta_S &= -\frac{1}{V}\left(\frac{\partial V}{\partial P}\right)_S \frac{\partial \rho}{\partial \rho} = -\frac{1}{V}\left(\frac{\partial \rho}{\partial P}\right)_S \frac{\partial V}{\partial \rho} = -\frac{1}{Vu_s^2}\frac{\partial V}{\partial \rho} \\
&= -\frac{1}{Vu_s^2}\frac{\partial(m/\rho)}{\partial \rho} = \frac{1}{\rho u_s^2}
\end{aligned}
\quad (2.3.7)
$$

Subsequently, (1.2.4) and (1.2.7) will finally result in

$$\kappa = \frac{C_P}{\rho u_s^2 C_V} \quad (1.2.8)$$

The right part (source term) of (2.2.14) will then become through (2.3.3) and (2.3.8)

$$-\frac{\beta}{\kappa u_s^2}\frac{\partial^2 T(\vec{r},t)}{\partial t^2} = -\frac{\beta}{C_P}\frac{\partial H(\vec{r},t)}{\partial t} \quad (2.3.9)$$

so that

$$\left(\nabla^2 - \frac{1}{u_s^2}\frac{\partial^2}{\partial t^2}\right)p(\vec{r},t) = -\frac{\beta}{C_P}\frac{\partial H(\vec{r},t)}{\partial t} \quad (2.3.10)$$

Additionally, $H(\vec{r},t)$ can be further decomposed as the product of the respective spatial and temporal parts in the following form

$$H(\vec{r},t) = H_S(\vec{r})H_T(t) \quad (2.3.11)$$

whereas $H_S(\vec{r})$ represents the local deposited energy density in J/m^3 and $H_T(t)$ is the temporal excitation profile (e.g. a Gaussian pulse).

Using (2.3.11), equation (2.3.10) can then be re-arranged as following

$$\left(\nabla^2 - \frac{1}{u_s^2}\frac{\partial^2}{\partial t^2}\right)p(\vec{r},t) = -\frac{\beta H_S(\vec{r})}{C_P}\frac{\partial H_T(t)}{\partial t} \quad (2.3.13)$$

comprising the photoacoustic equation under thermal confinement conditions.

In case that $H_T(t) = \delta(t)$ (i.e. impulse temporal excitation), we finally have

$$\left(\nabla^2 - \frac{1}{u_s^2}\frac{\partial^2}{\partial t^2}\right)p(\vec{r},t) = -\frac{\beta H_S(\vec{r})}{C_P}\frac{\partial \delta(t)}{\partial t} \quad (2.3.14)$$

2.4 Review of non-linear photoacoustics in literature

Several phenomena may induce nonlinear relationships between the photoacoustic signal amplitude and the energy of the incident light, such as optical saturation, temperature-dependence of thermodynamic parameters, photo-chemical reaction, or nano/micro-bubble formation [12]. Nonlinear phenomena could be on their own a means of selectively detect contrast agents, similarly as what is done in the field of ultrasound imaging. In the context of biomedical imaging, exploiting photoacoustic nonlinearity has been reported in a few recent works. In [13,14], the authors used nonlinear amplification of photoacoustic signals from laser-induced nano-bubbles.

In [13] their effort was focused on laser generation of nanobubbles as more efficient PA signal amplifiers from strongly absorbing, highly localized targets in the presence of spatially homogenous absorption background generating linear signals only. This approach was demonstrated by using nonlinear PA flow cytometry (PAFC) platform for label-free detection of circulating melanoma cells in blood background in vitro and in vivo. Specifically, nonlinearly

amplified PA signals from overheated melanin nanoclusters in melanoma cells became detectable above still linear blood background.
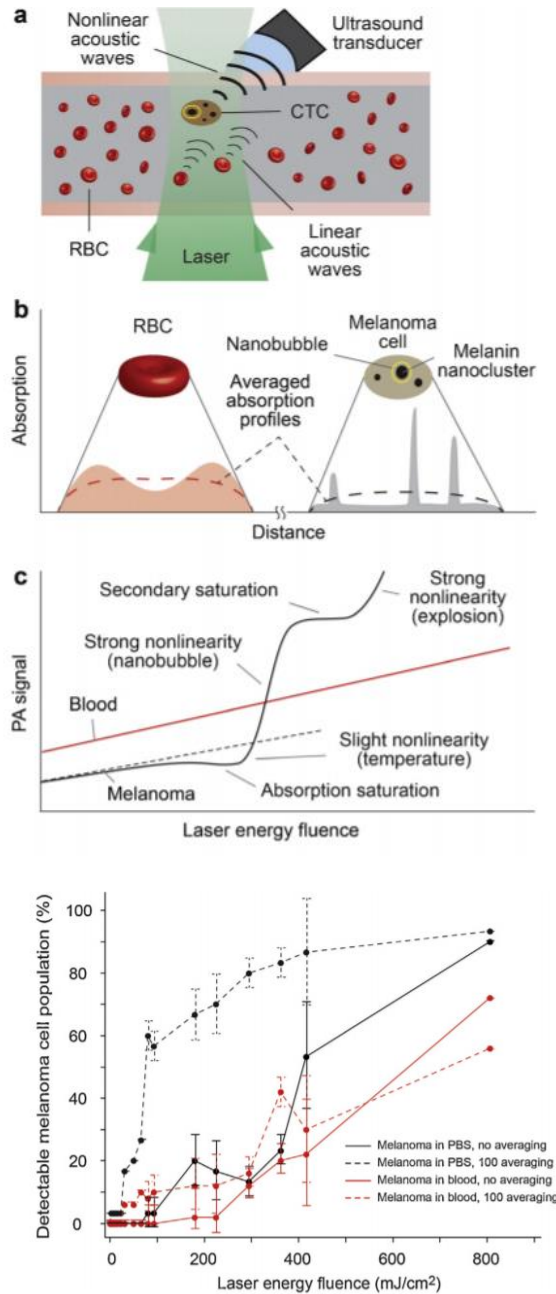
Figure 8: Principle of nonlinear PAFC. [13] (a) Schematics. (b) Absorption profiles of a red blood cell (RBC) and a melanoma cell. (c) Linear and nonlinear PA signal dependence on energy fluence from RBCs and melanoma cells. (d) Percentage of melanoma cell population that is detectable as function of laser fluence, under static conditions

In [14], they demonstrated the nonlinearity in photoacoustic signal from endocytosed gold nanoparticles. The photoacoustic signals from the tissue mimicking gelatin phantom containing inclusions of cells with endocytosed gold nanoparticles were quantitatively analyzed with respect to the cell/nanoparticle concentration and the laser fluence. Their study suggested that nonlinear photoacoustic signal increase from endocytosis of gold nanoparticles can be used in photoacoustic imaging to identify molecular/cellular interaction of plasmonic nanoparticles with cells.
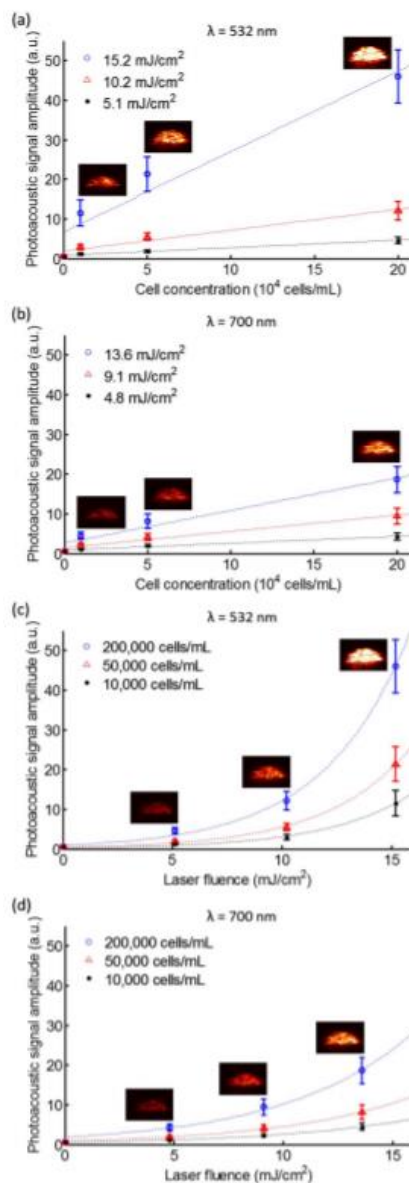
Figure 9: Photoacoustic signal amplitudes from the endocytosed gold nanoparticles in the tissue-mimicking phantom with respect to the cell concentration at wavelengths of (a) 532 nm

and (b) 700 nm and with respect to the laser fluence at wavelengths of (c) 532 nm and (d) 700 nm [14].

2.5 Physical mechanisms of non-linear photoacoustic effect

The nonlinear PA effects detected in our experiment arise from two major sources: nonlinear thermal expansion and optical absorption saturation [15]. When the mechanisms of photoacoustic pressure generation are generally considered, the rise of the local temperature by pulsed laser irradiation is often ignored with an assumption of constant thermophysical parameters (e.g., thermal expansion coefficient, density, speed of sound, and heat capacity). However, if the localized temperature rise is significant, it considerably alters the thermophysical parameters. Among the parameters related to the photoacoustic response, the thermal expansion coefficient is most dramatically changed as temperature increases. Based on this, there have been several studies to introduce the temperature dependent thermal expansion coefficient to simulate and explain the nonlinearity observed in photoacoustics. The thermal expansion coefficient, $\beta(T)$, can be generally considered as an intrinsic property of each material but when there is a temperature rise, T above the equilibrium temperature, T_0, it depends on this change of the temperature. When T is small,

$$\beta(T) \approx \beta_1 + \beta_2 T \quad 2.5.1$$

where β_1 and β_2 are the first two coefficients in the Taylor expansion around T_0.

If, the sample can be considered as acoustically homogenous and in addition, the laser pulse duration is sufficiently shorter than the transducer response time (several tens of nanoseconds), the photoacoustic excitation is considered to be in stress confinement within the acoustically defined resolution. In stress confinement, the initial volume-averaged temporal pressure rise, p_0, centered at $\sim \vec{r_0} = 0$ within the acoustic voxel V, is approximated by:

$$p_0 \approx \frac{1}{V_0 \kappa} \int_V \left[\beta_1 T(\vec{r}) + \frac{1}{2} \beta_2 (T(\vec{r}))^2 \right] \cdot d\vec{r} \quad 2.5.2$$

where κ is the isothermal compressibility and V_0 is a volume of size much larger than the distance between the absorbers.

The second major source of nonlinear PA effects detected is saturation of the optical absorption coefficient with increasing light intensity. For flat-top beam illumination, whose intensity is

constant in the lateral direction, the optical absorption coefficient of a homogenous sample within the laser beam can be expressed as a function of depth z and time t

$$\mu_a(z,t) \cong \frac{\mu_{a0}}{1+I(z,t)/I_{sat}} \quad 2.5.3$$

In the previous equation, $\mu_{a0} = \sigma \cdot N$ is the unsaturated optical absorption coefficient (m^{-1}), σ is the absorption cross section, N is the number of absorbers per unit volume, $I(z,t)$ is the intensity of the light beam at depth z at time t, and $I_{sat} = h\nu/\tau_r\sigma$ is the saturation intensity of the absorbing molecule, where τ_r is the absorption relaxation time, h is the Planck's constant, and ν is the frequency.

According to Beer's Law, in the presence of optical absorption, the optical intensity attenuates with depth, z. However, when the transducer's bandwidth is sufficiently large, Beer's Law attenuation has a negligible effect on the detected peak PA amplitude. Thus, at the sample surface, within the acoustic voxel, the intensity is approximated as time-varying only. In other words, $I(z,t) \approx I(0,t)$, and consequently, according to Eq. 2.4.3, the absorption coefficient becomes $\mu_a(z,t) \approx \mu_a(0,t)$.

To calculate the effects of thermal nonlinearity and optical saturation on the PA signal, we can consider the optical illumination in our experiments. The optical intensity at z=0 can be presumed to have the following general form:

$$I(z = 0,\vec{r},t) = E_p\widehat{f_s}(\vec{r})\widehat{f_t}(t) \quad 2.5.4$$

where, E_p is the pulse energy and $\widehat{f_s}(\vec{r})$ is the normalized spatial function. For a flat-top beam illumination, $\widehat{f_s}(\vec{r}) = \frac{1}{\pi R^2}rect(\frac{\vec{r}}{2R})$, where R is the beam radius and rect is a rectangular function. $\widehat{f_t}(t)$ is the normalized temporal function. For a Gaussian pulse, $\widehat{f_t}(t) = \frac{1}{\sqrt{2\pi}\tau_L}exp[-\frac{t^2}{2\tau_L^2}]$, where τ_L is a parameter related to the FWHM of the pulse. For a beam radius much larger than the acoustic wavelength, the intensity is considered to be constant in the lateral direction and $I(z = 0,\vec{r},t)$ is reduced to $I(z = 0,t)$.

For weak saturation (i.e. $I(z = 0,t) \ll I_{sat}$), the optical energy deposition (J/m^3) at the sample surface due to single photon absorption can be expanded in Taylor's series as:

$$A_e = \int_{-\infty}^{\infty} \mu_\alpha(0,t)I(0,t) \cdot dt \approx \mu_{\alpha0}I_{sat} \int_{-\infty}^{\infty}(\hat{I} - \hat{I}^2 + \hat{I}^3 \cdots +(-1)^{n-1} \cdot \hat{I}^n)dt \quad 2.5.5$$

where $\hat{I} = I(t)/I_{sat}$. For an incident beam with a Gaussian pulse, Eq. 2.5.5 becomes

$$A_e \approx \mu_{\alpha 0} F_{sat} \left(\sqrt{\frac{1}{1}} \hat{F} - \sqrt{\frac{1}{2}} \hat{F}^2 + \sqrt{\frac{1}{3}} \hat{F}^3 \cdots + (-1)^{n-1} \sqrt{\frac{1}{n}} \hat{F}^n \right) \quad 2.5.6$$

where $F_{sat} = \sqrt{2\pi} \tau_L I_{sat}$ and $\hat{F}$ is the incident fluence normalized by F_{sat}, $\hat{F} = F/F_{sat}$.

To evaluate the effect of thermal nonlinearity and optical saturation, we need to look at two different cases, namely, densely packed and loosely packed absorbers (Figure 10).
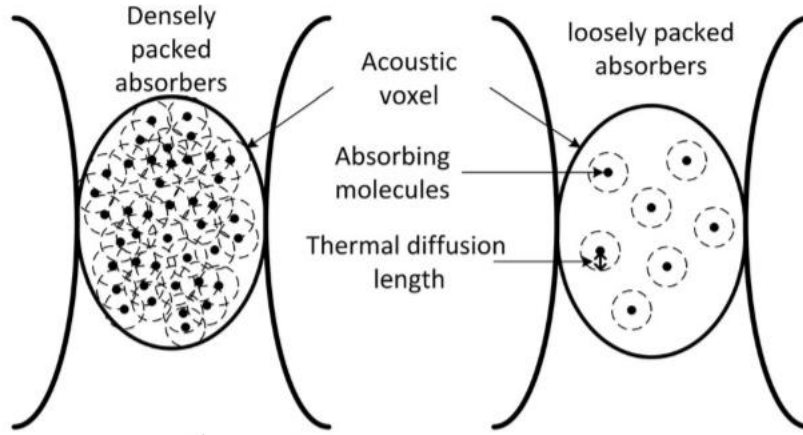
Figure 10: Densely and loosely packed absorbers within the acoustic voxel [15].

In densely packed molecules, the thermal diffusion length, $d_{th} = \sqrt{\chi \tau_L}$, where χ is the thermal diffusivity, is small compared to the dimensions of the acoustically and optically defined voxel, and large compared to the distance between absorbing molecules. Hence, the photoacoustic excitation is in macroscopic but not microscopic thermal confinement. Consequently, the absorbing area can be approximated by a continuous medium with a smooth temperature distribution, and the local temperature rise, T, is given by

$$T = \frac{\eta_{th} A_e}{\rho C_p} \quad 2.5.7$$

where η_{th} is the percentage of deposited optical energy that is converted into heat, ρ denotes the mass density, and C_p denotes the specific heat capacity at constant pressure. Thus, substituting Eqs. 2.5.7 and 2.5.6 into Eq. 2.5.2 yields:

$$p_0(F) = c_1 F + c_2 F^2 + \cdots \quad 2.5.8$$

Here, the linear coefficient is $c_1 = \Gamma\eta_{th}\mu_{a0}$, where Γ is the Grueneisen coefficient. For a flat-top spatial intensity profile and densely packed absorbers, the second-order coefficient as a function of the wavelength, λ, becomes:

$$c_2(\lambda) = \sigma^2(\lambda)(-\Gamma_1\eta_{th}\frac{N\tau_r(\lambda)}{hv\sqrt{2\pi}\tau_L(\lambda)} + \Gamma_2\eta_{th}^2 N^2) \quad 2.5.9$$

where, Γ_1 and Γ_2 are constants proportional to β_1 and β_2, respectively. The wavelength-dependent effects of thermal nonlinearity and optical saturation can be evaluated after the second-order coefficient, $c_2(\lambda)$, is scaled by dividing by the square of the absorption cross section, $\sigma^2(\lambda)$. The first term in $c_2(\lambda)/\sigma^2(\lambda)$ is negative and related to optical saturation. It is proportional to the absorption relaxation time of the molecule, $\tau_r(\lambda)$, and inversely proportional to the laser pulse width, $\tau_L(\lambda)$. Both parameters are wavelength-dependent. The second term in the $c_2(\lambda)/\sigma^2(\lambda)$ is positive, related to the thermal nonlinearity, constant at all wavelengths, and proportional to N^2.

For loosely packed molecules, the thermal diffusion length, d_{th}, is small compared to the distance between absorbing molecules (Figure 10). Hence, the photoacoustic excitation is in both macroscopic and microscopic thermal confinement. While the influence of optical saturation in the acoustic volume is the same, the contribution of thermal nonlinearity to the nonlinear PA signal is different. The heat distribution around each absorbing molecule is not affected by presence of other molecules. Hence, the thermal nonlinearity term in Eq. 2.5.9 is proportional to N rather than to N^2.

3. Materials and Methods

3.1 Experimental setup

The photoacoustic microscope we used for our measurements employed a variable repetition rate diode pumped ns laser (QIR-1064-200-S, CrystaLaser LC, Reno, NV, USA; energy per pulse: 29.4 μJ, pulse width: 10 ns, selected repetition rate: 5 kHz, M^2 value: ~1.2) emitting infrared irradiation at 1064 nm [16]. The beam was tightly focused by a lens on a Lithium Triborate (LBO) second harmonic generation crystal (Castech Inc, Fuzhou, China) to get a visible wavelength at 532 nm, which was used for the effective photoacoustic signal excitation. Following the LBO crystal, a second lens was employed in a telescopic configuration with the focusing one, collimating and expanding the beam by approximately two times. A bandpass filter (FF01-531/40-25, Semrock, Rochester, NY, USA), permitting the wavelength transmission from 511 to 551 nm, was subsequently placed to cut off the residual fundamental light. Using a couple of galvo mirrors system (Cambridge Technology, Micromax 6215H, Dual Servo Motor Drivers), the beam was guided into a properly modified inverted optical microscope (Labovert, Leitz, Wetzlar, Germany) serving as a platform for the developed imaging setup. The laser irradiation was further attenuated through a proper combination of neutral density filters in order to control the total energy deposition at the focal plane. A low numerical aperture (NA) objective lens (Achromat 8X, LOMO, St. Petersburg, Russia; air immersion, NA: 0.2) was employed for the focusing of the beam onto the specimen under investigation. The sample was fixed at the bottom of a custom-made, optically transparent tank, further attached on a set of sub-μm precision XY motorized stages (8MTF-75LS05, Standa, Vilinius, Lithuania) performing a lateral raster scanning as to the beam focus. The vertical position of the tubes was selected manually using the Z-adjustment microscope controls. The tank was filled with distilled water in order to provide an efficient acoustic coupling between the photoacoustic sources and the detection unit. A 20 MHz central frequency, spherically focused ultrasonic transducer (V373-SU, Olympus, Tokyo, Japan; effective bandwidth: approximately 13–33 MHz, focal distance: 32 mm) was immersed into the tank in a confocal and coaxial configuration with respect to the focal volume of the beam, achieving in this manner, the maximum detection sensitivity at the excited region. The detected broadband signals were additionally amplified using a low noise RF amplifier (AU-1291, Miteq, NY, USA; gain 63 dB)

connected to a computer. Furthermore, the signal was averaged 100 times at each measurement position for SNR improvement. The data acquisition triggering was provided by the control unit of the ns laser in order to synchronize the recording of the time-domain photoacoustic signal with the pulse incidence on the sample.
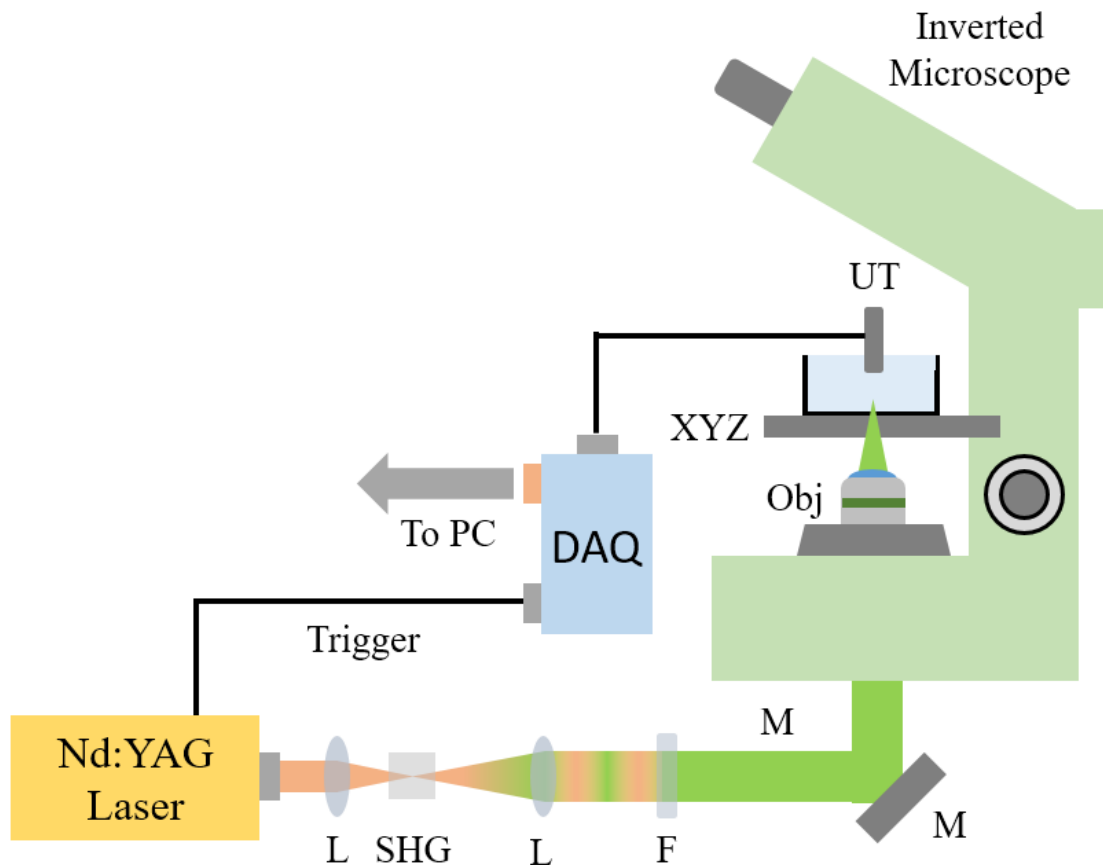

Figure 11: Schematics of OR-PAM system. L, lens; SHG, second harmonic generation crystal; F, filters; M, mirror; Obj, objective lens; UT, ultrasonic transducer; XYZ, motorized XY and manual Z stages; DAQ, data acquisition card

3.2 Sample preparation and experimental process

The aim of our study was to experimentally discriminate two different optical absorbers, exploiting the thermal nonlinearity of the generated photoacoustic signals, while using single wavelength excitation. In order to evaluate our claim, we required two samples, demonstrating distinct different nonlinear properties. After a broad bibliographical research we found that

black ink can serve as a strong nonlinear absorber [13]. On the other hand, mouse blood behaves almost linearly while the laser intensity increases. For this reason, we injected black ink and mouse blood inside transparent plastic tubes, as showed below, which were subsequently placed at the bottom of an optically transparent water tank. The experimental process was divided into two sections. The first section included spot measurements on the two absorbers for the purpose of determining their behavior as the laser intensity increases. The second section involves the differentiation between blood and ink through their nonlinear response. In particular, the final discrimination between them arises from the results of a custom made Matlab code, which enhances the contrast of the absorbers.
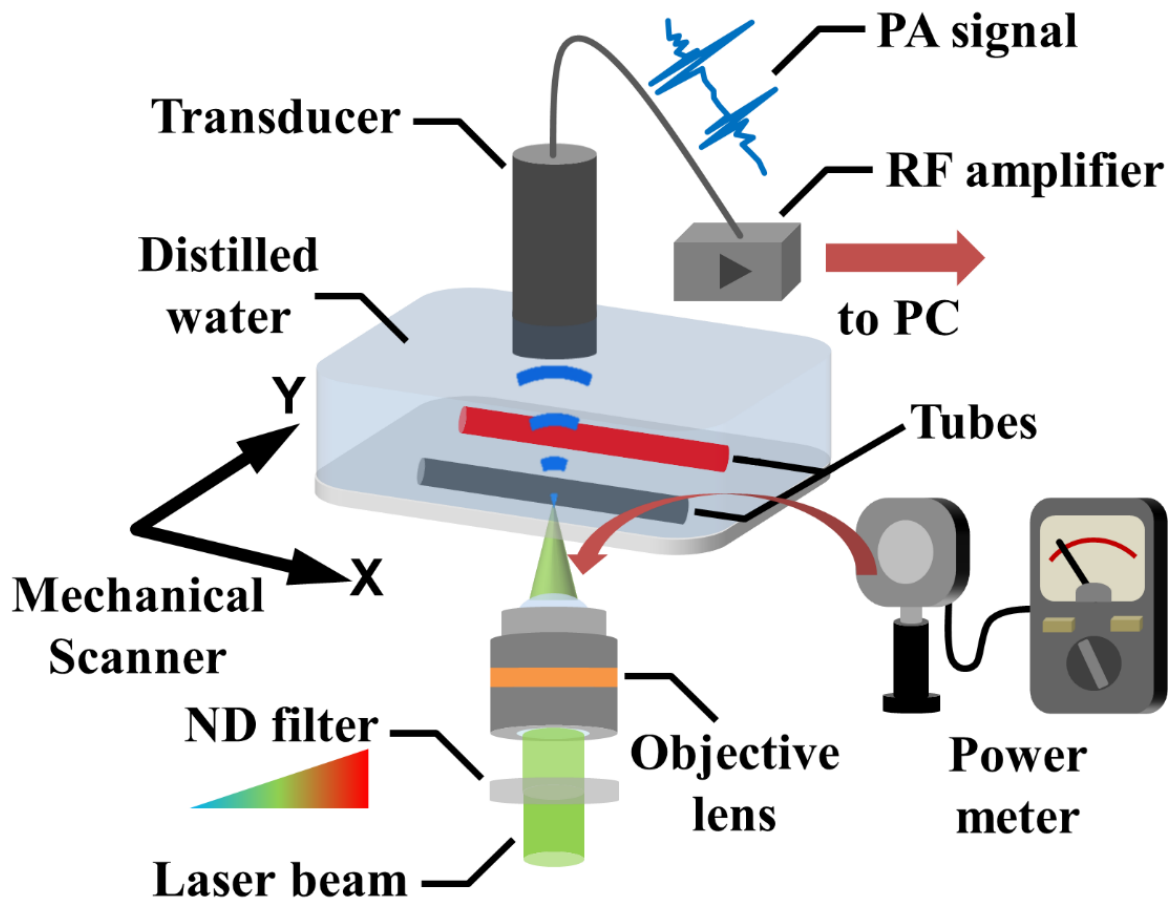
Figure 12: Experimental configuration for the realization of nonlinear PA measurements.

Figure 12 depicts the transparent tubes placed into the water tank filled with distilled water. The laser beam passes through the neutral density filters, which control the energy fluence deposited onto the samples, at the focal plane. After the filters, the objective lens focuses the beam, and

assuming that we have negligible losses at that point, the average power is measured by a power meter. A spherically focused ultrasonic transducer is immersed into the tank. The PA signal is averaged 100 times at each measurement position and after the amplification the signal is delivered to the PC.

4. Results

4.1 Spot measurements

The first step of the experimental process included the determination of the relation between photoacoustic response (PA signal) and energy fluence in blood and ink specimens through spot measurements. In particular, the sample was placed in the water tank and then the laser beam was focused at the plane of the tube. Neutral density filters were used in order to control the intensity of the light delivered on the specimen. In this manner, the power of the laser was gradually increasing and it was measured after the objective lens with a power meter, whereas the maximum PA signal amplitude was estimated by a custom-made software. The following graph (Figure 13) demonstrates the polynomially fitted (2nd order) experimental data recorded using mouse blood, diluted ink and pure ink as specimens.
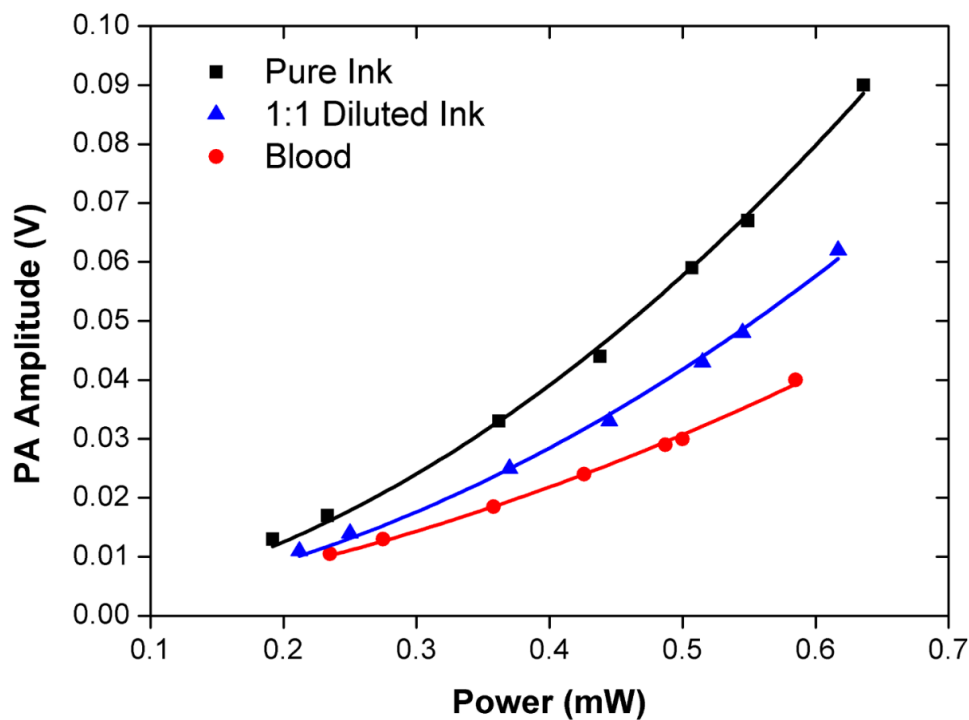
Figure 13: Combined graph of the non-linear PA response for three different absorbers.

In this graph, we can observe the obvious nonlinear behavior of the ink as a function of the applied energy fluence. Additionally, the higher the concentration of the ink the clearer this

behavior becomes. On the other hand, mouse blood seems to have an almost linear response as the power of the laser increases. In order to mathematically describe the previous data we used a polynomial fitting for each point series in the form of Ax+Bx^2, from which we extracted the linear and nonlinear coefficients for every sample.

	Blood	Diluted Ink	Pure Ink
Linear Coefficient (A)	0,02739±0,00183	0,02138±0,00256	0,02742±0,00529
Nonlinear Coefficient (B)	0,06798±0,00355	0,12434±0,00987	0,17587±0,01034

Table 1: Linear and non-linear coefficients for blood, diluted ink and pure ink.

We repeated this experiment several times and we made sure that the response of these 3 different samples is always the same with small differences as far as the coefficients are concerned. The next tables include our calculations of the coefficients and their errors, respectively. In addition, the mean value and the standard deviation for each coefficient are estimated.

Blood:

Linear Coefficient	Standard Error	Nonlinear Coefficient	Standard Error
0,02688	0,00179	0,06860	0,00440
0,02775	0,00363	0,06395	0,00729
0,02712	0,00494	0,06851	0,00959
0,02684	0,00419	0,07199	0,00854
0,02688	0,00258	0,06648	0,00529
0,02882	0,00333	0,05946	0,00674
0,02687	0,00223	0,06860	0,00464
Mean: 0,02731		**Mean:** 0,06680	
Standard deviation: 0,00740		**Standard deviation:** 0,00405	

Table 2: Linear and non-linear coefficients for multiple measurements for blood.

Diluted Ink:

Linear Coefficient	Standard Error	Nonlinear Coefficient	Standard Error
0,02612	0,00505	0,12137	0,01142
0,01872	0,00530	0,12470	0,01119
0,01863	0,00489	0,12246	0,01054
0,01798	0,00717	0,11741	0,01348
0,02086	0,00449	0,12496	0,00871
0,02634	0,00345	0,12012	0,00862
0,02219	0,00583	0,13083	0,01431
Mean: 0,02155		**Mean:** 0,12312	
Standard deviation: 0,00351		**Standard deviation:** 0,00429	

Table 2: Linear and non-linear coefficients for multiple measurements for diluted ink.

Pure Ink:

Linear Coefficient	Standard Error	Nonlinear Coefficient	Standard Error
0,02890	0,00718	0,17302	0,01471
0,02689	0,00508	0,17649	0,00969
0,02360	0,00959	0,18114	0,01854
0,02375	0,00800	0,18115	0,01471
0,02418	0,01348	0,18275	0,02550
0,02820	0,00691	0,17345	0,01470
0,02529	0,00965	0,16420	0,02010
Mean: 0,02583		**Mean:** 0,17602	
Standard deviation: 0,00753		**Standard deviation:** 0,00656	

Table 2: Linear and non-linear coefficients for multiple measurements for pure ink.

4.2 Absorber differentiation in OR-PAM through non-linear response exploitation

The next step, after completing the spot measurements, was to image pure ink and mouse blood samples using our photoacoustic microscope and discriminate the two absorbers based solely on their substantially different nonlinear properties. A custom-made MATLAB algorithm was used to process the images recorded at seven increasing energy fluences, and extract the magnitude of linear and non-linear contributions for each case.

More specifically, the blood and ink tubes were raster scanned over the focused laser beam to acquire 100 by 100 photoacoustic waveforms, which were translated into an image following a maximum amplitude projection of the signals. Great attention was given while placing the tubes into the water tank in order to be at the exact same level. This was necessary to assure that both of them receive the same local energy fluence and in turn that any difference at the absorption depends only on the intrinsic properties of each sample. Figure 14 shows the maximum amplitude projection (MAP) images of the tubes that were acquired for 0.282mW, 0.437mW and 0.593mW, respectively. Based on these values of the optical power, the pulse energy can be calculated by dividing the power with the repletion rate of the laser (5kHz). Consequently, the minimum pulse energy was 56.4 nJoule, whereas the maximum 118.6 nJoule. Additionally, the energy fluence can be calculated by dividing the pulse energy with the area covering the laser beam. The minimum energy fluence was 0.25 J/cm^2 and the maximum 0.53 J/cm^2.
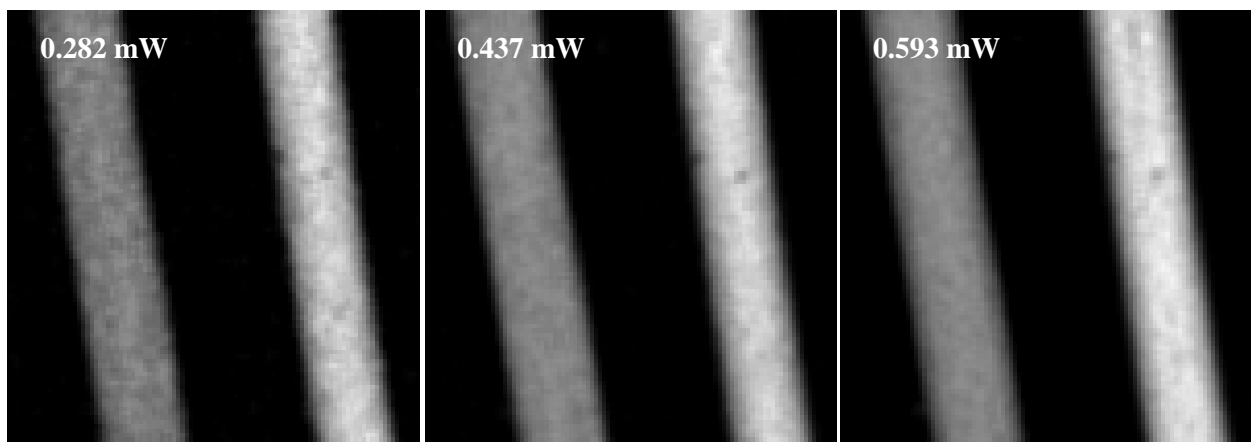
Figure 14: Maximum amplitude projection images of ink and blood.

We observe that as the power increases, the PA signal of the right tube becomes higher compared to the left tube. At this point, we could speculate that the right sample could be the ink, based on the results we acquired from the spot measurements, but still we cannot be sure about this assumption because the contrast between them is not high enough. The final discrimination between the two samples will be done after processing the data using the Matlab algorithm, explained in detail below. Heading to this direction, after running the Matlab code responsible for mapping the linear and nonlinear coefficients of the acquired data, we get the following 2D maps.
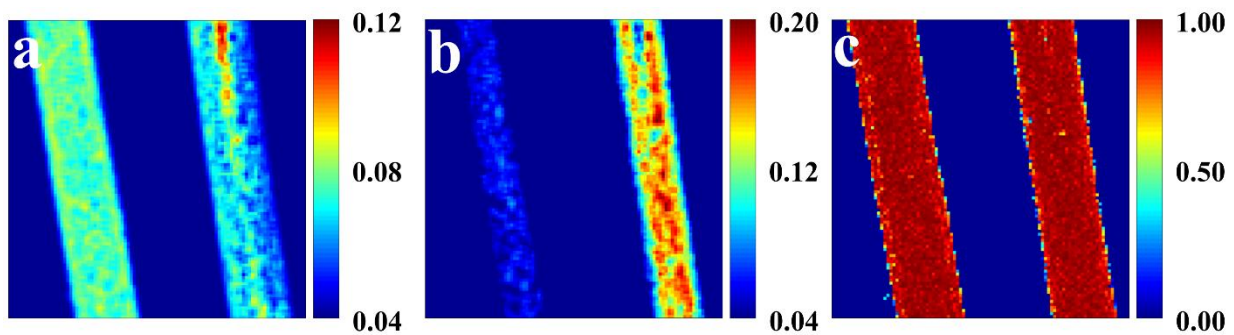
Figure 15: (a), (b): Maps of A (linear) and B (non-linear) coefficients extracted from the custom-made Matlab code, (c): R-squared evaluation for the fitting

In particular, the code initially loads the recorded maximum amplitude projection PA images, as well as, the seven corresponding optical power values measured before acquisition to form a 3D matrix of 100 X 100 X 7 elements. Following the arrangement of the data, the algorithm fits a 2nd order polynomial function, point by point, for the 10000 obtained PA measurements, having the form $Ax + Bx^2$, to determine the linear and nonlinear coefficients A and B. Hence, Figure 15a depicts the map of the linear coefficients A, whereas Figure 15b shows the distribution of nonlinear coefficients B. The quality of the fitting is very high, and this is shown explicitly in Figure 15c, where the R-squared values approach 1 for the experimental points corresponding to the tubes.

Regarding the left tube, we see that its linear coefficients are much higher compared to the respective nonlinear coefficient values, while the second tube reveals exactly opposite behavior. To further investigate the experimental results, we calculated the linear and nonlinear contribution of the photoacoustic signal for different powers. Using this data processing, we can

monitor the progress of these contributions gradually, while power is increased. Generally, the photoacoustic signal, P, can be described as
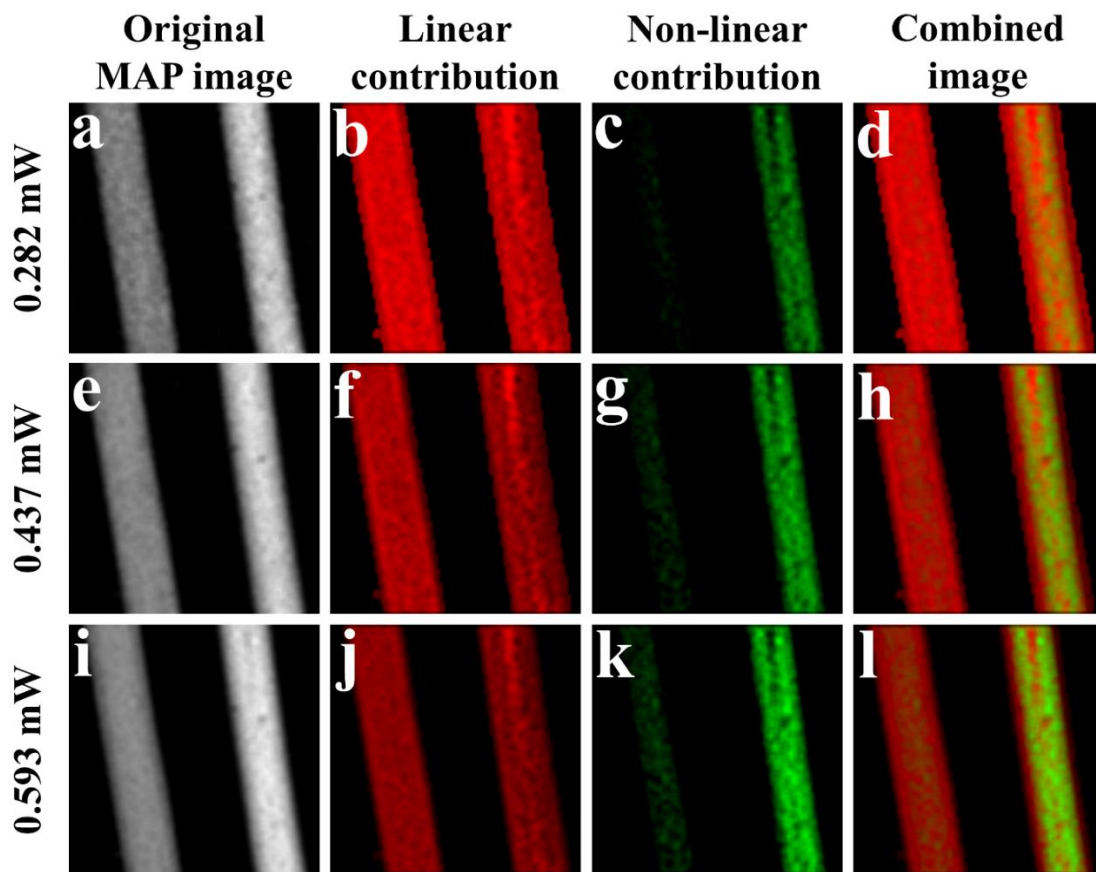
$$P \sim P_A + P_B$$

where $P_A = AF$ is the linear part of the PA signal and $P_B = BF^2$ is the 2nd order non-linear part. Hence, the total linear contribution is

$$\frac{P_A}{P_A + P_B} = \frac{AI}{AF + BF^2} = \frac{A}{A + BF}$$

while the non-linear contribution is

$$\frac{P_B}{P_A + P_B} = \frac{BF^2}{AF + BF^2} = \frac{BF}{A + BF}$$

Figure 16: (a), (e), (i): MAP images for different powers for mouse blood and ink, (b), (f), (j): Linear contribution of the PA signal for different powers, (c), (g), (k): Nonlinear contribution of the PA signal for different powers, (d), (h), (l): combined images of the linear and nonlinear contributions for different powers.

Considering these images, we see that at the starting point the linear contribution for both of the tubes has more or less the same value, but it fades as the laser power is increased. In fact, this decrease is more obvious for the second one. As far as the non-linear contribution is concerned, we observe that for the first tube it approaches zero and a small leap is revealed, as the power is increased. On the other hand, the non-linear contribution for the second tube is comparable with its linear contribution, in the beginning, but it becomes much more intense at high fluence values. If we combine the linear and nonlinear contribution, we get the final image, which again reveals which tube contains blood and which ink. Particularly, from the previous discussion we extract that the left tube is the blood, where the linear contribution outbalances, whereas the right one with the high non-linear contribution is the ink.

With the intention of evaluating the results of our new proposed method for unmixing based on the nonlinear properties of the optical absorbers, Figure 17 was generated in order to calculate the ratio of the intensities of the two absorbers, before and after the algorithmic process. The graph depicts the normalized pixel intensity profile across a line perpendicular to the two tubes.
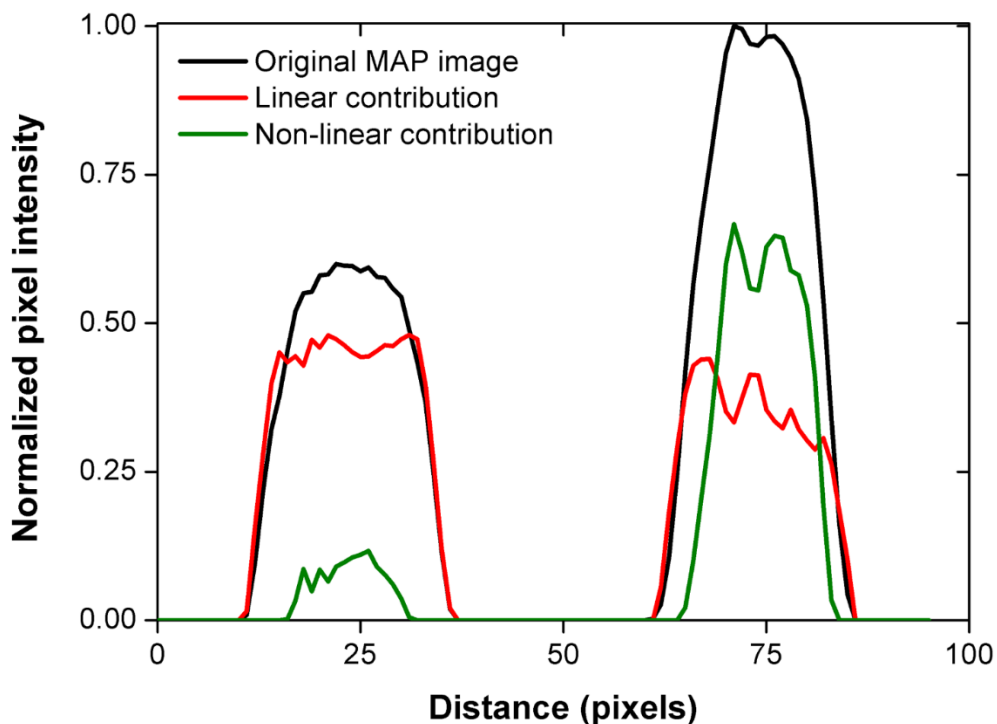
Figure 17: Normalized pixel intensity across the specimens

It is observed, that in the original MAP image, the contrast between ink and blood has a ratio of 1.64. Concerning the linear contribution, the ratio between the two intensities is calculated to be 0.8. This result was expected from the previous discussion because both of the absorbers appeared to have comparable linear response. On the other hand, the ratio of the two intensities for the nonlinear contribution is 6.74. Hence, we conclude that using the proposed non-linear PA methodology, we managed to dramatically enhance our imaging contrast by 4 times, being able to achieve a highly sensitive and reliable discrimination between the two absorbers.

5. Discussion and conclusions

In summary, we have a proposed a new method for discrimination of absorbers in OR-PAM using single wavelength excitation. Until now, at least two different excitation wavelengths had to be employed for the differentiation of optical absorbers, however in this study we have proven that by exploiting non-linear photoacoustic effects, a single wavelength can be used for this purpose.

Firstly, a set of spot measurements was performed on blood and ink tubes separately. This process revealed the intrinsic properties of these absorbers, regarding their PA response as a function of a gradually increasing energy fluence. Particularly, blood showed an almost linear response, whereas ink presented a high non-linear dependence of PA amplitude on the applied energy fluence. Taking advantage of their different behavior and with the intention of differentiating them, the specimens were subsequently raster scanned over the focused laser beam to acquire a series of photoacoustic waveforms, which were translated into an image following a maximum amplitude projection of the signals. At this point, the ratio of the amplitudes between ink and blood had a value of ~1.64. The experimental data was further processed by a custom-made MATLAB code for the calculation of the linear and non-linear contributions of the recorded PA signals at each image. Following the end of this procedure, the ratio of the respective pixel intensities in the extracted non-linear image was calculated to be significantly increased at ~6.74. Consequently, we managed to achieve a dramatic contrast enhancement between the two samples by a factor of ~4.1, demonstrating in this manner, the capabilities of OR-PAM in absorber differentiation using a single excitation wavelength.

The next goal of our study is to test different external contrast agents, showing high PA non-linearity, such as gold nanoparticles, and use them in imaging applications. Another application of great biological interest would be the differentiation between oxy- and deoxy-hemoglobin or the discrimination between hemoglobin and melanin, using non-linear effects in OR-PAM. Additionally, by taking into account the contribution of 3rd order non-linear effects, it would be potentially possible to discriminate three different absorbers based on their specific non-linear response.

To conclude, in this study we introduced a novel way for optical absorber unmixing in OR-PAM, based solely on their non-linear properties. This technique enhances both sensitivity and specificity in discriminating different samples. Finally, the proposed approach simplifies a lot the whole experimental process, since only a single laser wavelength is necessary, offering thus enhanced versatility and robustness, while retaining the total hardware cost at low levels.

References

[1]   Dominik Maximilian Soliman, Augmented microscopy: Development and application of high resolution optoacoustic and multimodal imaging techniques for label free biological application, 31-32

[2]   Paul Beard, Biomedical photoacoustic imaging, Interface Focus, 602–631, doi:10.1098/rsfs.2011.0028, (2011)

[3]   Brecht HP, Whole body three dimensional optoacoustic tomography system for small animals, Journal of Biomedical Optics, doi:10.1117/1.3259361, (2009)

[4]   Christopher P. Favazza, In vivo photoacoustic microscopy of human cutaneous microvasculature and a nevus, Journal of Biomedical Optics, doi:10.1117/1.3528661, (2011)

[5]   Song Hu, Second-generation optical-resolution photoacoustic microscopy with improved sensitivity and speed, Optics Letters, 1134-1136, (2011)

[6]   Geoffrey P. Luke, Optical wavelength selection for improved spectroscopic photoacoustic imaging, Photoacoustics, 36-42, (2013)

[7]   Daniel Razansky, Multispectral optoacoustic tomography of matrix metalloproteinase activity in vulnerable human carotid plaques, Molecular Imaging and Biology, 277-285, doi: 10.1007/s11307-011-0502-6, (2012)

[8]   Seungsoo Kim , In vivo three dimensional spectroscopic photoacoustic imaging for monitoring nanoparticle delivery, Biomedical Optics Express, 2540–2550, (2011)

[9]   Junjie Yao, Photoacoustic microscopy, Journal of Biomedical Optics, doi: 10.1002/lpor.201200060, (2011)

[10]   Christian Lutzweiler, Optoacoustic Imaging and Tomography: Reconstruction Approaches and Outstanding Challenges in Image Performance and Quantification, Sensors, 7345-7384, doi:10.3390/s130607345, (2013)

[11]   Lihong V. Wang, Biomedical Optics principles and imaging

[12]   Olivier Simandoux, Influence of nanoscale temperature rises on photoacoustic generation: Discrimination between optical absorbers based on thermal nonlinearity at high frequency, Photoacoustics, 20-25, doi: 10.1016/j.pacs.2014.12.002, (2015)

[13]   Mustafa Sarimollaoglu, Nonlinear photoacoustic signal amplification from single targets in absorption background, Photoacoustics, 1-11, (2014)

[14]   Seung Yun Nam, Nonlinear photoacoustic signal increase from endocytosis of gold nanoparticles, Optics Letters, 4708-4710, (2012)

[15]   Amos Danielli, Nonlinear photoacoustic spectroscopy of hemoglobin, Applied Physics Letters, (2015)

[16]   Tserevelakis G, Hybrid photoacoustic and optical imaging of pigments in vegetative tissues, Journal of microscopy, doi: 10.1111/jmi.12396, (2016)